Draft version September 27, 2016
Preprint typeset using LaTeX style AASTeX6 v. 1.0

arXiv:1603.08921v2 [astro-ph.SR] 25 Sep 2016

TURBULENT CHEMICAL DIFFUSION IN CONVECTIVELY BOUNDED CARBON FLAMES

Daniel Lecoanet[1,2], Josiah Schwab[1,2], Eliot Quataert[1,2], Lars Bildsten[3,4], F. X. Timmes[3,5], Keaton J. Burns[6], Geoffrey M. Vasil[7], Jeffrey S. Oishi[8], & Benjamin P. Brown[9]

[1]Physics Department, University of California, Berkeley, CA 94720, USA
[2]Astronomy Department and Theoretical Astrophysics Center, University of California, Berkeley, CA 94720, USA
[3]Kavli Institute for Theoretical Physics, University of California, Santa Barbara, CA 93106, USA
[4]Department of Physics, University of California, Santa Barbara, CA 93106, USA
[5]School of Earth and Space Exploration, Arizona State University, Tempe, AZ 85287, USA
[6]Department of Physics, Massachusetts Institute of Technology, Cambridge, Massachusetts 02139, USA
[7]School of Mathematics & Statistics, University of Sydney, NSW 2006, Australia
[8]Department of Physics & Astronomy, Bates College, Lewiston, ME 04240
[9]Laboratory for Atmospheric and Space Physics and Department of Astrophysical & Planetary Sciences, University of Colorado, Boulder, Colorado 80309, USA

ABSTRACT

It has been proposed that mixing induced by convective overshoot can disrupt the inward propagation of carbon deflagrations in super-asymptotic giant branch stars. To test this theory, we study an idealized model of convectively bounded carbon flames with 3D hydrodynamic simulations of the Boussinesq equations using the pseudospectral code Dedalus. Because the flame propagation timescale is much longer than the convection timescale, we approximate the flame as fixed in space, and only consider its effects on the buoyancy of the fluid. By evolving a passive scalar field, we derive a *turbulent* chemical diffusivity produced by the convection as a function of height, $D_t(z)$. Convection can stall a flame if the chemical mixing timescale, set by the turbulent chemical diffusivity, D_t, is shorter than the flame propagation timescale, set by the thermal diffusivity, κ, i.e., when $D_t > \kappa$. However, we find $D_t < \kappa$ for most of the flame because convective plumes are not dense enough to penetrate into the flame. Extrapolating to realistic stellar conditions, this implies that convective mixing cannot stall a carbon flame and that "hybrid carbon-oxygen-neon" white dwarfs are not a typical product of stellar evolution.

1. INTRODUCTION

Super-asymptotic giant branch (SAGB) stars are characterized by the development of a degenerate carbon-oxygen (CO) core and the subsequent ignition of off-center carbon fusion within it. Stellar evolution calculations show that this occurs in stars that have zero-age main sequence masses $\approx 7 - 11\,M_\odot$, with this mass range depending on the metallicity and on modeling assumptions such as the mass loss rate and the efficiency of mixing at convective boundaries. Carbon ignition initially occurs as an off-center flash, but after one or more of these flashes, a self-sustaining carbon-burning front can develop (see e.g., Siess 2006; Farmer et al. 2015). This "flame" propagates towards the center of the star extremely sub-sonically, as heat from the burning front is conducted inward. The heat from the burning also drives a convective zone above the burning front, and in the quasi-steady-state, the energy released by carbon fusion is balanced by energy losses via neutrino cooling in this convective zone (Timmes et al. 1994). As the carbon-burning flame propagates to the center, it leaves behind oxygen-neon (ONe) ashes. This process creates the core that will become a massive ONe WD or collapse to a neutron star, powering an electron-capture supernova (Miyaji et al. 1980).

However, the presence of additional mixing near the flame can lead to its disruption, preventing carbon burning from reaching the center. There are at least two physical processes that may play a role in this region: (1) mixing driven by the thermohaline-unstable configuration of the hot ONe ash on top of the cooler CO fuel and (2) mixing driven by the presence of a convective zone above the flame via convective overshoot. These processes were investigated by Denissenkov et al. (2013) using 1D stellar evolution models. With a thermoha-

dlecoanet@berkeley.edu

line diffusion coefficient informed by multi-dimensional hydrodynamics simulations, they concluded that thermohaline mixing was not sufficient to disrupt the flame. However, they did find that the introduction of sufficient convective boundary mixing—using a model of exponential overshooting (Freytag et al. 1996; Herwig 2000)—disrupted the flame, preventing carbon burning from reaching the center. This led to the production of "hybrid C/O/Ne" WDs, in which a CO core is overlaid by an ONe mantle. Several groups have begun to model the explosions that would originate from objects with this configuration (Denissenkov et al. 2015; Kromer et al. 2015; Bravo et al. 2016; Willcox et al. 2016).

Is mixing sufficiently vigorous to disrupt the carbon flame? This is a key question for understanding the final outcomes of SAGB stars and the WDs they produce. If the thermal diffusivity κ is much larger than the chemical diffusivity D, the flame propagates into fresh fuel much more quickly than the fuel and ash can mix, allowing the flame to successfully propagate to the center of the star. We estimate $\kappa/D \sim 10^6$ using the thermal conductivity in MESA (which is drawn from Cassisi et al. 2007) and a chemical diffusivity from Beznogov & Yakovlev (2014). However, convective mixing could produce a *turbulent* diffusivity D_t, which if similar to κ, could mix ash into the fuel, stalling the flame, as was found in Denissenkov et al. (2013).

In this paper, we present 3D simulations of an idealized model of a convectively-bounded carbon flame. These simulations allow us to measure the enhanced mixing due to convective overshoot, and to determine if $D_\mathrm{t} > \kappa$ within the flame. Section 2 summarizes the properties of carbon flames, which we use to motivate the problem setup presented in Section 3. Section 4 presents the results of our simulations and we discuss their implications in Section 5.

2. CARBON FLAME PROPERTIES

To obtain an example of the structure of a carbon flame, we evolve a star with zero-age main sequence mass of 9.5 $\mathrm{M}_\odot$ using revision 6794 of the MESA stellar evolution code[1] (Paxton et al. 2011, 2013, 2015). We used the publicly available inlists of Farmer et al. (2015), who undertook a systematic study of carbon flames in SAGB stars. We did not include the effects of overshoot at the convective boundaries, but did include the effects of thermohaline mixing. The Brunt-Väisälä (buoyancy) frequency profile of the carbon flame is shown by the blue line in Fig. 1. The thermal component dominates the buoyancy frequency. The much smaller compositional component is destabilizing, but Denissenkov et al. (2013) found thermohaline mixing to not affect flame propagation. The flame structure in Fig. 1 is similar to that shown in Figure 3 of Denissenkov et al. (2013).

The peak of the buoyancy frequency profile shown in Fig. 1 is at a Lagrangian mass coordinate of $M_r = 0.13\,\mathrm{M}_\odot$. The properties of the flame change as it propagates, but the following numbers are representative throughout the evolution. The inward flame velocity is $u = 9 \times 10^{-4}\,\mathrm{cm\,s^{-1}}$; it will take $\sim 10^4\,\mathrm{yr}$ to reach the center. The flame width, δ, measured in terms of pressure scale height, $H = 2 \times 10^8\,\mathrm{cm}$, is $\delta/H \approx 0.03$. The timescale for the flame to cross itself, $t_\mathrm{cross} = \delta/u \approx 200\,\mathrm{yr}$, which is also the timescale for the nuclear burning to occur. The convection zone above the flame has a radial extent of about one pressure scale height and a convective turnover timescale of a few hours. This implies that there are $\sim 10^5$ convective turnover times in the time it takes flame to cross itself. Thus, over the relatively smaller number of convective turnover times covered by our simulations, $\sim 10^2$, the flame is effectively stationary, allowing us to exclude nuclear reactions in our model.

We note that our stationarity assumption is not universally applicable. Convectively bounded oxygen-neon-burning flames, which can also occur in the late evolution of stars in this mass range are thinner, $\delta \sim 10^3\,\mathrm{cm}$, and have higher velocities, $u \sim 1\,\mathrm{cm\,s^{-1}}$, as a result of the higher energy generation rate (Timmes et al. 1994; Woosley & Heger 2015). Consequently, the time for the flame to traverse its width may be $\lesssim 10$ convective turnover times. Thus it is difficult to anticipate how our simulations carry over to the case of oxygen-neon flames.

The Mach number of the convection is $\approx 4 \times 10^{-5}$, so compressibility does not play an important role in the convection. To measure the degree of turbulence of the convection, we calculate the Rayleigh number

$$\mathrm{Ra} = \frac{\omega_0^2 H^4}{\nu\kappa}, \tag{1}$$

which is the ratio of convective driving to diffusive damping. The variables ω_0 and H represent typical convective frequencies and lengths, and ν and κ are the kinematic viscosity and thermal diffusivity. We estimate the convection driven by a carbon flame to have $\mathrm{Ra} \sim 10^{24}$, using $\omega_0 \sim 3 \times 10^{-4}\,\mathrm{s^{-1}}$, $H \sim 2 \times 10^8\,\mathrm{cm}$, $\nu \sim 5 \times 10^{-2}\,\mathrm{cm^2\,s^{-1}}$ (Itoh et al. 1983) and $\kappa \sim 3 \times 10^3\,\mathrm{cm^2\,s^{-1}}$ (Itoh et al. 1987). This large Rayleigh number means the flow is extremely turbulent.

Flames maintain coherence because their thermal diffusivity is much larger than their chemical diffusivity. The ratio of these diffusivities is the Lewis number

$$\mathrm{Le} = \frac{\kappa}{D}. \tag{2}$$

[1] MESA is available at http://mesa.sourceforge.net/.

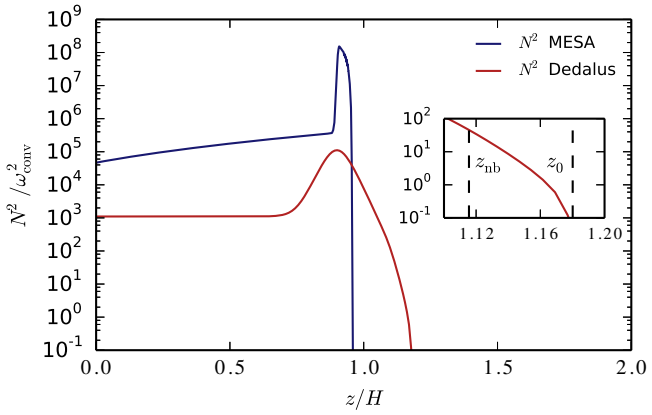

Figure 1. The blue line shows the buoyancy frequency squared near a carbon flame from a 9.5 $M_\odot$ star evolved in MESA. The red line is the buoyancy frequency squared from the Dedalus simulation R8 (very close to its initial profile, see equation 6). Due to computational limitations, the buoyancy frequency in the model of the carbon flame is much lower and the transition between the buoyancy peak and the convective region is much more gradual, in Dedalus than in the MESA model. These differences both act to enhance the convective mixing via overshoot in Dedalus. The inset shows the neutral buoyancy height $z_{\rm nb}$ and the bottom of the convection zone z_0 in the Dedalus simulation. In the MESA model, this region is not resolved, with a width $z_0 - z_{\rm nb} < 3 \times 10^{-3} H$.

For carbon flames, we estimate Le $\sim 10^6$.

3. PROBLEM SETUP

Our idealized simulations make a variety of assumptions to render this problem computationally tractable. We do not include nuclear reactions because the flame is effectively stationary on the convection time scale. We use the Boussinesq approximation because the Mach number of the convection is small, and the height of the convection zone is about a scale height, so we do not believe density contrasts across the convection zone will strongly alter the dynamics.

3.1. *Equations, Numerics, & Assumptions*

We solve the 3D Boussinesq equations (Spiegel & Veronis 1960) using the Dedalus[2] pseudo-spectral code (Burns et al. 2017).

$$\partial_t \boldsymbol{u} + \boldsymbol{\nabla} p - \nu \nabla^2 \boldsymbol{u} - g T \boldsymbol{e}_z = -\boldsymbol{u} \cdot \boldsymbol{\nabla} \boldsymbol{u}, \quad (3)$$

$$\partial_t T - \kappa \nabla^2 T = -\boldsymbol{u} \cdot \boldsymbol{\nabla} T + \bar{H}, \quad (4)$$

$$\boldsymbol{\nabla} \cdot \boldsymbol{u} = 0, \quad (5)$$

where $\boldsymbol{u}$ and p are the fluid velocity and pressure, respectively, T is the temperature normalized to a reference value, g is the gravitational acceleration, and $\boldsymbol{e}_z$ is the unit vector in the vertical direction. We neglect the compositional effects on buoyancy (and thus thermohaline mixing), and always use $\nu = \kappa$ for computational convenience.

Convective overshoot is particularly sensitive to the buoyancy frequency profile (e.g., Brummell et al. 2002). Thus, we study convective overshoot using a buoyancy frequency profile inspired by a carbon flame. This assumes that the most important property affecting turbulent mixing of a carbon flame is its strong buoyancy stabilization.

The simulations are initialized with a temperature profile $T_0(z)$ satisfying $N_0^2(z) = g \mathrm{d}T_0/\mathrm{d}z$, where

$$N_0^2 = -\omega_0^2 + N_{\rm tail}^2 \frac{1}{2}\left[1 - \tanh\left(\frac{z - z_{\rm fl}}{\Delta z_{\rm fl}}\right)\right] + N_{\rm fl}^2 \cosh\left(\frac{z - z_{\rm fl}}{\Delta z_{\rm fl}}\right)^{-2}, \quad (6)$$

where ω_0^2 is a characteristic convective frequency, and we take $N_{\rm tail}^2 = 100\omega_0^2$, $N_{\rm fl}^2 = 10^4 \omega_0^2$ as approximations to the MESA model. The position of the buoyancy peak ("flame") is $z_{\rm fl} = 0.9H$ and its half-width is $\Delta z_{\rm fl} = 0.05H$, where H represents a pressure scale height. We plot the time-averaged buoyancy frequency profile of simulation R8 in Fig. 1 with a red line. All simulations have very similar buoyancy frequency profiles, which differ from N_0^2 only very close to the bottom of the convection zone. We also include a heating term $\bar{H} = -\kappa \partial_z^2 T_0$ which exactly balances the diffusion of T_0. This maintains the buoyancy profile and convection over the course of our simulations, enforcing the stationary assumption.

It is important to note that a flame with the width and thermal diffusivity used in our simulations would propagate across itself in only 10^{1-2} convective turnover times. This is because the thermal diffusion in the simulations is much more rapid than in a star. As a result, the stationary buoyancy peak in our simulations does not self-consistently represent a real carbon flame, whose properties would depend on the thermal diffusivity. However, in the limit in which the thermal diffusivity in the simulation approaches the thermal diffusivities realized in stars, the simulations would provide a good approximation to convective overshoot in real carbon flames. Therefore, we hold the buoyancy profile of the model "flame" fixed as we carry out simulations with different microphysical diffusivities. We show below that despite the need to extrapolate the simulation results, we can nonetheless draw firm conclusions about convective mixing in carbon flames.

The simulations are non-dimensionalized using the pressure scale height H, and the initial buoyancy frequency in the convection zone $|N_0(z = 2H)| = \omega_0$. These are used to define a Rayleigh number (Eqn. 1). The limited resolution of any multi-dimensional astro-

[2] Dedalus is available at http://dedalus-project.org.

physics simulation requires diffusivities much larger than in stars, so we can only reach $\mathrm{Ra} = 10^9 \ll 10^{24}$. Our highest resolution simulation required about 3 million cpu-hours on the Pleiades supercomputer.

We define the bottom of the convection zone, where $N^2 = 0$, to be z_0. We also define the height of neutral buoyancy $z_{\rm nb}$, the point at which $\langle T(z_{\rm nb})\rangle_{x,y,t} = \langle T(z_{\rm top})\rangle_{x,y,t}$, where $\langle\cdot\rangle_x$ denotes an average over x, and $z_{\rm top}$ is the top of the domain (see inset in Fig. 1). Plumes emitted at the top of the convection zone become neutrally buoyant at $z_{\rm nb}$. Convective plumes cross z_0, but rarely pass below $z_{\rm nb}$.

The convection frequency $\omega_{\rm conv}$ and the height of the convection zone $H_{\rm conv}$ are outputs of the simulation. We define $H_{\rm conv}$ using z_0 and

$$\omega_{\rm conv} = 2\pi \frac{w_{\rm rms}}{H_{\rm conv}}, \tag{7}$$

where $w_{\rm rms}$ is the root-mean-square vertical velocity in the convection zone. We find $H_{\rm conv} \approx 0.83H$ and $\omega_{\rm conv} \sim 0.3\omega_0$.

Simulations with higher Ra have smaller $\omega_{\rm conv}$. This is driven by the thermal equilibration of the system. In statistically steady state, the convection zone is almost isothermal, so the temperature perturbation at the bottom of the convection zone is about $-H_{\rm conv}\omega_0^2/g$. To satisfy our bottom boundary condition, the stable region has a temperature gradient of about $-H_{\rm conv}\omega_0^2/(gH_{\rm stable})$, where $H_{\rm stable} = 2 - H_{\rm conv}$. Because the temperature gradient in the stable region is independent of κ, the heat flux scales like $\kappa \sim \mathrm{Ra}^{-1/2}$. To maintain flux balance, this heat flux must be carried by the convective flux in the convection zone, which scales like $w_{\rm rms}^3$. Thus, we have that $w_{\rm rms} \sim \omega_{\rm conv} \sim \mathrm{Ra}^{-1/6}$.

Plumes become neutrally buoyant at $z_{\rm nb}$, but will penetrate further due to their inertia. To measure this effect, we define an "overshoot number" Ov, which is the ratio of inertial to buoyancy forces near $z_{\rm nb}$,

$$\mathrm{Ov} \equiv \frac{\omega_{\rm conv}^2}{N_{\rm fl}^2}\frac{\Delta z_{\rm fl}}{H}, \tag{8}$$

where we estimate the inertia of the fluid as $\sim \omega_{\rm conv}^2 H$, and the buoyancy as $H^2 N_{\rm fl}^2/\Delta z_{\rm fl}$. The latter assumes the derivative of the buoyancy frequency squared near $z_{\rm nb}$ is proportional to $N_{\rm fl}^2/\Delta z_{\rm fl}$. We report Ov for our simulations in Table 1.

For comparison, we estimate real flames have $\mathrm{Ov} \sim 10^{-10}$, using $N_{\rm fl}^2 \sim 2\times 10^8$ and $\Delta z_{\rm fl} = 0.03H$. However, the buoyancy frequency profile is actually much steeper than this linear estimate, so the real Ov is likely even smaller (see Fig. 1). Our chosen buoyancy profile differs from the MESA model in two important ways: (1) the peak is at lower frequencies; and (2) the buoyancy frequency approaches zero more gradually. This is necessary because it is difficult to resolve the fast buoyancy timescale, and sharp buoyancy gradients numerically. Both these changes lead to substantially higher Ov than we expect in real flames. Thus, we expect our simulated plumes to penetrate much further than the convective plumes driven by carbon flames. Table 1 also reports the Reynolds number, a measure of the degree of turbulence in the fluid, defined as

$$\mathrm{Re} = \frac{w_{\rm rms}H_{\rm conv}}{\nu}. \tag{9}$$

We solve the equations in cartesian geometry (x, y, z), in the domain $[0, 4H]^2 \times [0, 2H]$. The simulations are periodic in the horizontal directions, and no-slip with zero temperature perturbation at the top and bottom. All quantities are expanded in a Fourier series in the horizontal directions. In the vertical direction, quantities are independently expanded in Chebyshev polynomials over the domain $[0, 1.05H]$, and over the domain $[1.05H, 2H]$, with boundary conditions imposed at $z = 1.05H$ to maintain continuity of each quantity and its first vertical derivative. An equal number of Chebyshev modes are used in each vertical sub-domain. 3/2 dealiasing is used in each direction. We use mixed implicit-explicit timestepping, where all the linear terms are treated implicitly, and the remaining terms treated explicitly. The timestep size is determined using the Courant–Friedrichs–Lewy (CFL) condition. Table 1 describes the simulations presented in this paper.

3.2. *Passive Tracer Field*

The goal of this work is to estimate turbulent diffusivities associated with convective overshoot. To do this, we solve for the evolution of a passive tracer field c

$$\partial_t c - D\nabla^2 c = -\boldsymbol{u}\cdot\boldsymbol{\nabla} c. \tag{10}$$

The tracer c heuristically represents the fuel concentration, and D is a proxy for chemical diffusivity (and is required for numerical stability). The tracer c satisfies zero flux boundary conditions on the top and bottom of the domain, so its volume integral is conserved. It is initialized with

$$c = \frac{1}{2}\left[1 - \tanh\left(\frac{z - 0.8H}{\Delta z_{\rm fl}}\right)\right], \tag{11}$$

which corresponds to $c = 0$ in the convection zone and $c = 1$ below the buoyancy peak in the stable region.

4. RESULTS

After several convective turnover times, the system reaches a statistically steady state. We visualize the convection in Fig. 2, plotting 2D vertical slices of the temperature perturbation field and the normalized passive scalar field. The temperature perturbation is $T' =$

Table 1. List of simulations. The Rayleigh and Lewis number characterize the diffusion in the simulations (see eqns. 1 & 2). The resolution is the number of Fourier or Chebyshev modes used in each direction. The CFL safety factor is listed along with our choice of timestepper. The overshoot number Ov measures the ratio of inertial to buoyancy forces in the overshoot region (see eqn. 8). The Reynolds number describes the degree of turbulence in the simulation (see eqn. 9). The three columns after the Reynolds number are the heights at which $D_t = \alpha\kappa$, where $\alpha = 1$, 0.3, or 0. For comparison, in simulation R8, the bottom of the convection zone is $z_0 = 1.180$ and the height of neutral buoyancy is $z_{nb} = 1.116$. The last column is the overshoot length (normalized to the pressure scale height H), defined as the distance between the bottom of the convection zone and the location where $D_t = 0$.

Name	Ra	Le	Resolution	Timestepper/CFL	Ov	Re	$D_t = \kappa$	$D_t = 0.3\kappa$	$D_t = 0$	L_{ov}
R7	10^7	1	256^3	RK222[a]/1.0	4×10^{-4}	150	1.123	1.097	1.066	0.111
R8	10^8	1	256^3	RK222/1.0	2×10^{-4}	329	1.122	1.102	1.080	0.101
R9	10^9	1	512^3	SBDF2[b]/0.4	1×10^{-4}	751	1.122	1.107	1.091	0.090
R7L3	10^7	$10^{1/2}$	256^3	RK222/1.0	4×10^{-4}	150	1.133	1.102	1.061	0.116
R8L3	10^8	$10^{1/2}$	256^3[c]	RK222/1.0	2×10^{-4}	329	1.133	1.109	1.083	0.098
R7L10	10^7	10	256^3[c]	RK222/1.0	4×10^{-4}	150	1.145	1.111	1.063	0.114

[a]Second order, two-stage Runge-Kutta method (Ascher et al. 1997)

[b]Second order semi-backward differencing (Wang & Ruuth 2008).

[c]The passive scalar field is evolved at 512^3.

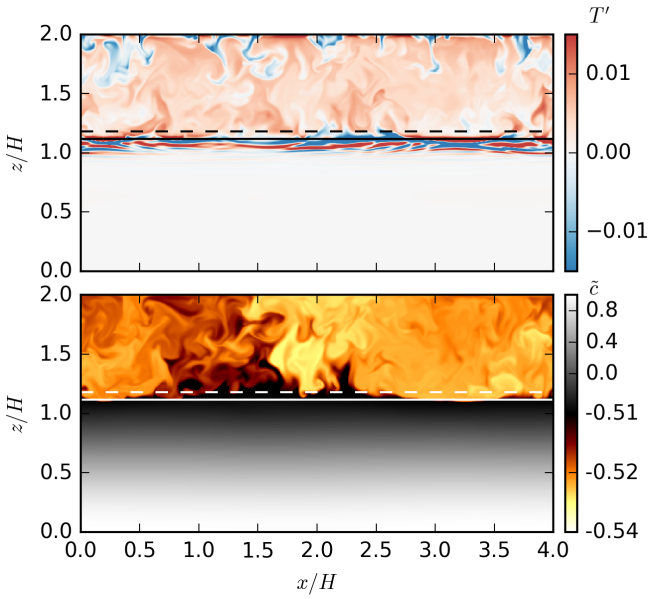

Figure 2. Two dimensional vertical slices of the temperature perturbation field (top) and the normalized passive scalar field (bottom) in simulation R9. The color scale for $\tilde{c}$ consists of two linear maps, stitched together at $\tilde{c} \approx -0.5$ to show the small variations within the convection zone. The dashed line shows the bottom of the convection zone, z_0, and the solid line shows z_{nb} the neutral buoyancy height. The perturbations below z_{nb} are waves and yield negligible mixing.

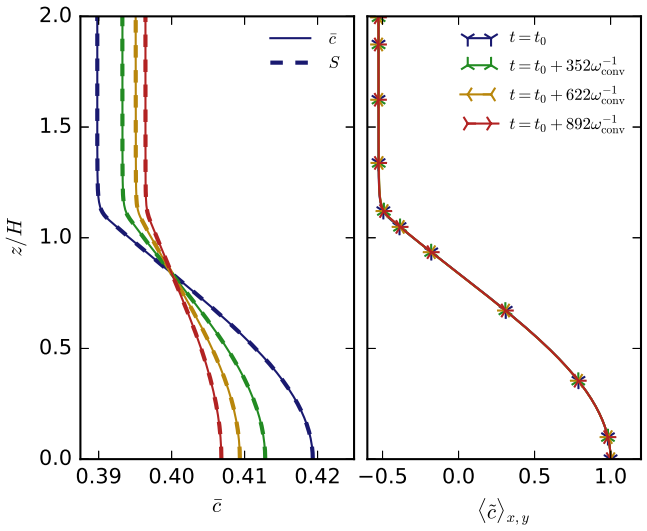

Figure 3. Horizontal average of the passive scalar field at four times in simulation R8. $\bar{c}$ is also time-averaged around each time for $30\omega_{conv}^{-1}$. The passive scalar field is attracted to the self-similar solution, C (right panel and equation 13). The left panel also shows the solution of the effective diffusion model (equation 16). The 1D effective diffusion model matches the 3D simulation.

$T - \langle T \rangle_{x,y,t}$. We normalize the passive scalar field by subtracting off the volume-average, and setting its value to 1 at the bottom boundary:

$$\tilde{c} = (c - \langle c \rangle_{x,y,z}) \,/\, (\langle c(z=0) \rangle_{x,y} - \langle c \rangle_{x,y,z}) \quad . \tag{12}$$

Fig. 2 includes dashed lines at the bottom of the convection zone, z_0, and solid lines at the height of neutral buoyancy z_{nb}. There is substantial convective overshoot between z_0 and z_{nb}. Below z_{nb}, the buoyancy perturbations show the long, coherent structures of internal gravity waves. These waves yield negligible mixing.

4.1. *Self-Similar Solution*

We now study the evolution of the horizontal average of the passive scalar field, $\bar{c} \equiv \langle c \rangle_{x,y}$. After several convective turnover times, $\bar{c}$ approaches a self-similar solution. The left panel of Fig. 3 shows the evolution of $\bar{c}$ in simulation R8, where t_0 is several turnover times after the beginning of the simulation. The profiles collapse to a single curve after subtracting off the volume-average

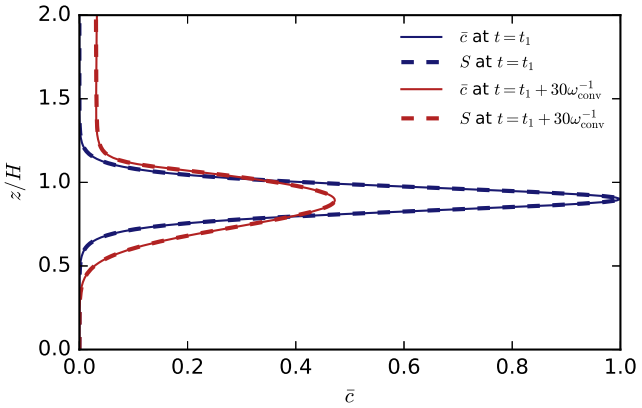

Figure 4. Horizontal average of a passive scalar field using the convection in simulation R8. c is initialized at t_1 to be horizontally uniform, with the vertical profile shown here. The diffusion model equation (16) was initialized with the same profile. The 1D effective diffusion model matches the 3D simulation over the entire simulation.

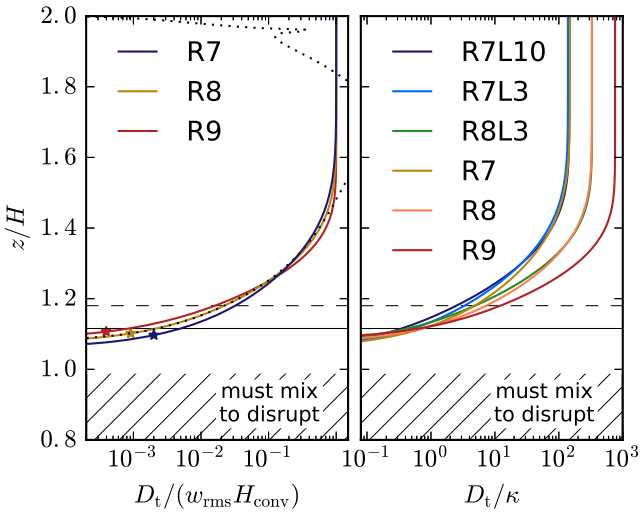

Figure 5. Turbulent diffusivity (equation 15) as a function of height in each of our simulations, both in units of the characteristic convective diffusivity (left panel), and in units of the thermal diffusivity (right panel). We plot a fit to $D_{\rm t}$ for all simulations, and also plot $|D_{\rm t}|$ itself in the thin dotted line for simulation R8. The dashed line shows the bottom of the convection zone, z_0, and the solid line shows $z_{\rm nb}$, the neutral buoyancy height. In the left panel, the height at which $D_{\rm t} = 0.3\kappa$ is marked by an asterisk—mixing can only affect flame propagation above this point. The hatched region shows the region that must be mixed in order to disrupt the flame (section 4.4). Increasing Ra and/or Le causes $D_{\rm t}$ to approach zero further away from the buoyancy peak, meaning that mixing is less significant for more realistic parameters.

and normalizing the bottom value to unity (i.e., taking the horizontal average of $\tilde{c}$ shown in Fig. 2). This indicates that

$$\bar{c}(z,t) - \langle \bar{c} \rangle_z \to A(t)C(z), \tag{13}$$

where $A(t)$ is an amplitude, and $C(z)$ the vertical profile in the right panel of Fig. 3. Furthermore, we find that $A(t) = A_0 \exp(-\lambda t)$. C thus satisfies the equation

$$-\lambda C - D\partial_z^2 C = -\left\langle \boldsymbol{u} \cdot \boldsymbol{\nabla} \frac{c}{A} \right\rangle_{x,y,t} \tag{14}$$

We now assume that the term on the right hand side can be written as a turbulent diffusion term. This is the Fickian diffusion ansatz (e.g., Brandenburg et al. 2009). The equation can be rewritten as

$$-\lambda C = \partial_z \left[(D + D_{\rm t}) \partial_z C \right], \tag{15}$$

where $D_{\rm t}(z)$ is a turbulent diffusivity profile. We can invert equation (15) to solve for $D_{\rm t}$ in terms of λ and C by integrating the equation with respect to z and then dividing by $\partial_z C$. We find that $D_{\rm t} \ll D$ in the stable region, and is large $\sim w_{\rm rms} H_{\rm conv}$ in the convection zone; the value of $D_{\rm t}$ is not well-constrained in the convection zone, as $\partial_z C$ is very close to zero. We find that the *effective* diffusivity, $D + D_{\rm t}$ is well-fit by two error functions, one which varies from zero in the convection zone to D in the stable region, the other which varies from zero in the stable region to $w_{\rm rms} H_{\rm conv}$ in the convection zone. In the rest of this paper, we replace $D_{\rm t}$ by a least-squares fit composed of these error functions. Fig. 5 (left panel) includes both $|D_{\rm t}|$ (dotted black line) and the least-squares fit (yellow line) for simulation R8.

4.2. *Turbulent Diffusivity Model*

To show that the convection acts like a turbulent diffusivity, we solve the model equation

$$\partial_t S(z,t) = \partial_z \left[(D + D_{\rm t}) \partial_z S(z,t) \right]. \tag{16}$$

If we initialize $S(z,t)$ with $\langle c(t = t_0) \rangle_{x,y}$ and use our fit for $D_{\rm t}(z)$, we find that $S \approx A(t)C(z)$, as shown in Fig. 3, for every simulation.

As a further test of the diffusion model, we re-initialized simulation R8 with a new concentration field profile halfway through the simulation at time t_1. We solved equation (16) with $S(z,t_1) = \bar{c}(t = t_1)$. Fig. 4 shows that $S \approx \bar{c}$ for the remainder of the simulation.

4.3. *Diffusion Profiles*

We plot the turbulent diffusion profiles $D_{\rm t}(z)$ for each of our simulations in Fig. 5, both in units of the characteristic convective diffusivity (left panel), and in units of the thermal diffusivity (right panel). In the convection zone, the diffusivity is about equal to the convective diffusivity, partially dictated by our choice of fit. The turbulent diffusivity drops from its convective value *within* the convection zone. This cannot be attributed to the change in the horizontal average of w^2 near z_0 (similar to Jones et al. 2016). Deep within the stably stratified region, the turbulent diffusivity is nearly zero.

We are interested in how $D_{\rm t}$ transitions from large

values in the convection zone to small values in the stable region. In this respect, the behavior of D_t/κ is very similar in all simulations (Fig. 5, right panel). Heuristically, we expect mixing to play a role in the propagation of flames when $D_t \sim \kappa$. We find that the height at which $D_t = \kappa$ is almost independent of Ra, but increases with Le (Table 1), i.e., moves closer to the convective boundary and further from the "flame." In section 4.4, we find that a more precise criterion for flame disruption is $D_t \gtrsim 0.3\kappa$ in the region in which $N \gtrsim 0.1 N_{\rm fl}$. The height at which $D_t = 0.3\kappa$ increases with both Ra (Fig. 5, left panel), and Le (Table 1), suggesting that flame disruption becomes less likely for more realistic values of Ra and Le

Two common parameterizations of convective overshoot are exponential overshoot, in which the turbulent diffusivity drops exponentially with distance from the end of the convection zone (e.g., Herwig 2000), and an overshoot length, in which the convective diffusivity is set to zero at a length $L_{\rm ov}$ beyond the convection zone (e.g., Shaviv & Salpeter 1973; Maeder 1975). In all our simulations, D_t is *negative* below a critical height (although the *effective* diffusivity $D + D_t$ is everywhere positive). This suggests that a good parameterization of our simulations would be an overshoot length, rather than exponential overshoot. We define the overshoot length $L_{\rm ov}$ to be the distance between the bottom of the convection zone (where $N^2 = 0$), and the location where $D_t = 0$, and report it in Table 1. All lengths in the paper, including $L_{\rm ov}$ are normalized to the pressure scaleheight H. Below the point at which $D_t = 0$ the absolute value of D_t is very small.[3]

The weak dependence of D_t in the overshoot region on the diffusivities of the system suggests that the height at which $D_t = 0.3\kappa$ and the overshoot length $L_{\rm ov}$ are determined primarily by the length scale on which the buoyancy frequency profile changes from zero to order ω_c, rather than a diffusive length scale. This suggestions that the key lengthscale in the problem is $\sim z_{\rm nb} - z_0$ (see Fig. 1). Indeed, the overshoot lenght $L_{\rm ov} \sim z_{nb} - z_0$ in all of our simulations (Table 1). This is because dense plumes falling through the convection zone become much lighter than their surroundings below $z_{\rm nb}$, so they cannot penetrate much further to produce mixing within the flame. We expect the overshoot length to scale as

$$L_{\rm ov} - (z_0 - z_{\rm nb}) \sim {\rm Ov}^{1/3}. \tag{17}$$

[3] We cannot place strong constraints on $|D_t|$ when its value is very small, as its value can be influenced by some combination of: 1. Timestepping errors due to using a low ($2^{\rm nd}$) order timestepper; or 2. Errors in the calculation of $C(z)$ or λ due to insufficient averaging.

Our simulations do not explore a sufficiently wide range of Ov to test this scaling. Although increasing Ra or Le further will introduce smaller eddies into simulations, we do not believe these smaller eddies will enhance mixing, as they are subject to the same buoyancy barrier as the larger plumes resolved in the simulations presented here.

4.4. *Flame Disruption in MESA*

We explore the secular effects of mixing on flame propagation via a series of numerical experiments using MESA. We begin with the evolution of a $9.5\,{\rm M}_\odot$ star (the same calculation discussed in Section 2). We save a model when the carbon flame is at a Lagrangian mass coordinate of $0.2\,{\rm M}_\odot$. We load this model in revision 8118 of MESA and use the built-in `other_D_mix` routine to introduce an artificial chemical diffusivity in the vicinity of the flame. We then observe whether this additional mixing affects the behavior of the flame. In the absence of additional mixing, the carbon-burning luminosity in the flame is smooth (in time) and roughly constant, with some secular variation as the flame propagates inward. We evolve the MESA models for $\approx 2000\,{\rm yr}$, which is $\approx$ 10 self-crossing times for the flame; in this time, the unperturbed flame propagates inwards through $\approx 0.1\,{\rm M}_\odot$ of material. We classify the flame as "disrupted" if the carbon-burning luminosity decreases significantly (by more than a factor of ≈ 10) or exhibits oscillatory behavior (by more than ≈ 10 %).

First, we set the chemical diffusivity (D_t) roughly equal to the convective diffusivity, $10^{12}\,{\rm cm^2\,s^{-1}}$ (which is $\sim H^2\omega$), in the region of the flame where $N < N_{\rm crit}$. This allows us to determine the region where significant mixing is required to disrupt the flame. Increasing $N_{\rm crit}$ increases the amount of material in which additional mixing occurs, similar to increasing the overshoot length scale.[4] We find the flame is only disrupted if $N_{\rm crit} \gtrsim 0.3 N_{\rm fl}$, where $N_{\rm fl}$ is the peak of the buoyancy frequency. This reflects the fact that it is necessary to mix material in the region where the bulk of the nuclear energy release is occurring in order to disrupt the flame.

Second, we set the chemical diffusivity to be a constant factor times the thermal diffusivity over a region where $N < N_{\rm crit}$. This allows us to determine the ratio D_t/κ needed to disrupt a flame. In terms of the opacity $\kappa_\star$, the thermal diffusivity is given by

$$\kappa = \frac{4acT^3}{\kappa_\star \rho^2 c_{\rm P}} \tag{18}$$

where a is the radiation constant, c the speed of light, T the temperature, ρ the density, and $c_{\rm P}$ the specific

[4] However, unlike overshooting, the mixing that we introduce is not spatially tied to the convective boundary.

heat at constant pressure. For a value of $N_{\rm crit} = 0.3N_{\rm fl}$, we find that the flame is only disrupted if $D_t > 0.3\kappa$. This agrees with our heuristic that $D_{\rm t} \sim \kappa$ is necessary for flame disruption. If the mixing is allowed to be even deeper into the flame (higher $N_{\rm crit}$), lower diffusivities are required; however, because our simulations suggest the turbulent diffusivity drops off very sharply with depth, we believe the most germane requirement for flame disruption is that from the shallowest mixing.

We use the criteria derived from these MESA calculations to interpret the results of our Dedalus simulations. The Dedalus simulations address where and how efficiently convection mixes material in the presence of a buoyancy barrier. However, because they do not self-consistently model a conductively-propagating flame, they cannot directly answer the question of whether a flame disrupts. The MESA calculations directly address whether convective mixing with a specific efficiency (relative to κ) and at a specific location (relative to N) is sufficient to disrupt a flame. We show these criteria in Fig. 5: the region where $N > 0.3N_{\rm fl}$ is hatched and the points where $D_{\rm t} = 0.3\kappa$ are marked with stars. In all our Dedalus simulations, the stars are outside the hatched region, which implies that the mixing observed in Dedalus would not be sufficient to disrupt the flame.

5. CONCLUSIONS

This paper describes simulations of an idealized model of convectively bounded carbon flames. The simulations are in the Boussinesq approximation, and assume a Brunt-Väisälä frequency profile motivated by MESA simulations of carbon flames (Fig. 1). On the convective timescale, carbon flames are almost stationary, so we do not explicitly include any nuclear burning in our model.

The simulations evolve a passive scalar field which heuristically represents the carbon species fraction. Overshooting plumes mix the passive scalar into the convection zone. The passive scalar field quickly approaches a self-similar solution (equation 13; see Fig. 3), allowing us to calculate an effective diffusivity profile $D_{\rm t}(z)$. The horizontally averaged 3D evolution of the passive scalar field is very well approximated by the solution of a 1D diffusion equation (equation 16; see Fig. 4).

Our simulations have large diffusivities compared to real stars. Despite the unphysical parameter regime of our simulations, we believe that we can still draw strong conclusions about mixing in real carbon flames, because of the clear trends in the simulation results as the parameters become more realistic, i.e., with increasing Rayleigh and Lewis numbers.

Carbon flames have $\kappa/D \sim 10^6$, but convective mixing can stall a flame if the turbulent mixing due to overshoot is such that $D_{\rm t} \sim \kappa$ within the flame. Overshoot in 1D stellar models is sometimes modeled by exponentially decreasing the diffusion coefficient outside the convection zone over a characteristic length (e.g., Herwig 2000). This parameterization does not in fact apply to our simulations, which have turbulent diffusivities which decrease as Gaussians, and then become negative below a critical height (Sec. 4.3). This suggests that a more useful parameterization is an overshoot length, as we find no convective mixing below a critical height.

MESA calculations suggest that a region near the peak of the buoyancy frequency ($N \sim 0.3N_{\rm fl}$) must be mixed with $D_{\rm t} > 0.3\kappa$ in order to disrupt the flame (Sec. 4.4). None of our simulations of convective overshoot show any convective mixing in this region. In all of our simulations, the height at which $D_{\rm t} = 0.3\kappa$ is well outside the region near the peak of the buoyancy frequency that MESA simulations show must be mixed in order to stall the flame (Fig. 5). Moreover, this height shifts closer and closer to the convection zone (away from the flame) as either the Rayleigh number or κ/D (the Lewis number) increase towards more realistic values.

Furthermore, our simulations greatly overestimate the mixing efficiency, as our buoyancy frequency increases only modestly with depth (Fig. 1). Although the ratio of inertia in our convective plumes to the stabilizing buoyancy force is very small ($\sim 10^{-4}$; see Table 1), we estimate that our simulated plumes are nonetheless more powerful than realistic plumes by a factor of at least $\sim 10^6$.

Taken together, these results strongly suggest that convection provides insufficient mixing to disrupt real carbon flames. The only way out of this conclusion is to posit that for yet higher Ra or Le numbers, the trends we find in mixing with increasingly realistic parameters reverse. Although we cannot rule this out, we regard it as unlikely. Physically, the lack of mixing is due to a simple physical principle: convective plumes must overcome a huge buoyancy barrier to reach the flame. There is no reason to expect them to suddenly be able to do so at even higher Ra or Le. As a result, we conclude that convection provides insufficient mixing to disrupt a carbon flame and that "hybrid C/O/Ne" WDs are unlikely to be a typical product of stellar evolution.

We have neglected important physics in this work, including rotation, magnetism, density stratification, and nuclear burning. However, it seems difficult for these effects to overcome the potential energy barrier, so we do not believe they will change our conclusion.

Internal gravity waves generated by the convection could mix the fluid via breaking. The wave amplitude increases as $\sqrt{N}$ as the waves leave the convection zone and approach the flame. Waves can break if $k_r \xi_r \sim 1$, where ξ_r is the vertical displacement and k_r is the vertical wavenumber. Neglecting damping, theoretical models of internal wave generation by convection

(e.g., Lecoanet & Quataert 2013) claim $k_r \xi_r \sim 1$ at the peak of the buoyancy frequency, $N_{\rm fl}$. However, the waves linearly damp due to thermal diffusion (which does not lead to chemical mixing). For carbon flames, we estimate the linear damping to become important near $N_{\rm fl}$, so it is unclear if the waves would break. Furthermore, breaking waves may only mix the unburnt fuel near $N_{\rm fl}$, having little effect on flame propagation.

Our simulations all have $\nu = \kappa$, but in stars, we estimate the Prandtl number $\mathrm{Pr} = \nu/\kappa \sim 10^{-5}$. Thus, there are small-scale motions which are isothermal, but not strongly influenced by viscosity. These motions can penetrate the buoyancy gradient in the flame, and thus are expected to enhance mixing. At a fixed Pr, we expect mixing to become less efficient as Ra increases, as the length scale on which perturbations are isothermal will decrease. Thus, as Ra increases, there will be less and less energy in isothermal perturbations.

More quantitatively, the largest length scale for isothermal perturbations is $\ell \sim \kappa/v_\ell$, where v_ℓ is typical velocity of eddies of size ℓ. Assuming a Kolmogorov cascade with $v_\ell \sim \omega_0 H (\ell/H)^{1/3}$, we have $v_\ell \sim 3 \times 10^2\,\mathrm{cm\,s^{-1}}$ and $\ell \sim 10\,\mathrm{cm}$. The diffusive mixing produced by these eddies is about $D_\mathrm{t} \sim \ell v_\ell \sim \kappa$, which is enough to disrupt the flame. However, these eddies will travel a depth $\ell \ll \delta$, and thus should not penetrate far enough into the flame to disrupt it. Future work should validate these estimates.

Given the strong intermittency of convective turbulence, it is also possible that the majority of overshoot mixing may be caused by a few rare but powerful plumes. Although our study cannot rule out this possibility, we note that there are about $\sim 10^6$ convective turnover times in the lifetime of a carbon flame. This is many fewer turnover times than in other astrophysical contexts (e.g., the solar convection zone), so rare events may be less important for carbon flames.

Future work should also study mixing via overshoot in oxygen-neon flames, which is important for understanding whether stars at the top of the SAGB mass range undergo Fe core collapse or electron-capture-induced ONe core collapse (Jones et al. 2014).

ACKNOWLEDGMENTS

We thank two anonymous referees for elucidating comments. We acknowledge stimulating workshops at Sky House where these ideas germinated. D.L. is supported by the Hertz Foundation. E.Q. is supported in part by a Simons Investigator Award from the Simons Foundation. J.S. is supported by NSF grant AST 12-05732. G.M.V. acknowledges support from the Australian Research Council, project number DE140101960. J.S.O. is supported by a Provost's Research Fellowship from Farmingdale State College. This research is funded in part by the Gordon and Betty Moore Foundation through Grant GBMF5076 to L.B. and E.Q. Resources supporting this work were provided by the NASA High-End Computing (HEC) Program through the NASA Advanced Supercomputing (NAS) Division at Ames Research Center. This project was supported by NASA under TCAN grant number NNX14AB53G. This work was partially supported by the National Science Foundation under grants PHY 11-25915 and AST 12-05574.

REFERENCES

Ascher, U. M., Ruuth, S. J., & Spiteri, R. J. 1997, Appl. Numer. Math., 25, 151
Beznogov, M. V., & Yakovlev, D. G. 2014, PhRvE, 90, 033102
Brandenburg, A., Svedin, A., & Vasil, G. M. 2009, MNRAS, 395, 1599
Bravo, E., Gil-Pons, P., Gutiérrez, J. L., & Doherty, C. L. 2016, ArXiv e-prints, arXiv:1603.00641
Brummell, N. H., Clune, T. L., & Toomre, J. 2002, ApJ, 570, 825
Burns, K. J., Vasil, G. M., Oishi, J. S., et al. 2017, In preparation
Cassisi, S., Potekhin, A. Y., Pietrinferni, A., Catelan, M., & Salaris, M. 2007, ApJ, 661, 1094
Denissenkov, P. A., Herwig, F., Truran, J. W., & Paxton, B. 2013, ApJ, 772, 37
Denissenkov, P. A., Truran, J. W., Herwig, F., et al. 2015, MNRAS, 447, 2696
Farmer, R., Fields, C. E., & Timmes, F. X. 2015, ApJ, 807, 184
Freytag, B., Ludwig, H.-G., & Steffen, M. 1996, A&A, 313, 497
Herwig, F. 2000, A&A, 360, 952
Itoh, N., Kohyama, Y., & Takeuchi, H. 1987, ApJ, 317, 733
Itoh, N., Mitake, S., Iyetomi, H., & Ichimaru, S. 1983, ApJ, 273, 774
Jones, S., Andrassy, R., Sandalski, S., et al. 2016, ArXiv e-prints, arXiv:1605.03766
Jones, S., Hirschi, R., & Nomoto, K. 2014, ApJ, 797, 83
Kromer, M., Ohlmann, S. T., Pakmor, R., et al. 2015, MNRAS, 450, 3045
Lecoanet, D., & Quataert, E. 2013, MNRAS, 430, 2363
Maeder, A. 1975, A&A, 40, 303
Miyaji, S., Nomoto, K., Yokoi, K., & Sugimoto, D. 1980, PASJ, 32, 303
Paxton, B., Bildsten, L., Dotter, A., et al. 2011, ApJS, 192, 3
Paxton, B., Cantiello, M., Arras, P., et al. 2013, ApJS, 208, 4
Paxton, B., Marchant, P., Schwab, J., et al. 2015, ApJS, 220, 15
Shaviv, G., & Salpeter, E. E. 1973, ApJ, 184, 191
Siess, L. 2006, A&A, 448, 717
Spiegel, E. A., & Veronis, G. 1960, ApJ, 131, 442
Timmes, F. X., Woosley, S. E., & Taam, R. E. 1994, ApJ, 420, 348
Wang, D., & Ruuth, S. J. 2008, J. Comput. Math., 26, 838
Willcox, D. E., Townsley, D. M., Calder, A. C., Denissenkov, P. A., & Herwig, F. 2016, ArXiv e-prints, arXiv:1602.06356
Woosley, S. E., & Heger, A. 2015, ApJ, 810, 34